Crop Classification Using Multi-Temporal RADARSAT Constellation Mission Compact Polarimetry SAR Data

Classification des cultures à l'aide de données multitemporelles radar à synthèse d'ouverture en mode polarimétrie compacte de la Mission de la Constellation RADARSAT

Ramin Farhadiani, Saeid Homayouni, Avik Bhattacharya & Masoud Mahdianpari

Published online: 20 Aug 2024.

Submit your article to this journal ☒

View related articles ☒

View Crossmark data ☒

Taylor & Francis
Taylor & Francis Group

Crop Classification Using Multi-Temporal RADARSAT Constellation Mission Compact Polarimetry SAR Data

Classification des cultures à l'aide de données multitemporelles radar à synthèse d'ouverture en mode polarimétrie compacte de la Mission de la Constellation RADARSAT

Ramin Farhadiani[a]*, Saeid Homayouni[a], Avik Bhattacharya[b], and Masoud Mahdianpari[c]

[a]Centre Eau Terre Environnement, Institut National de la Recherche Scientifique, Quebec City, Quebec, Canada; [b]Microwave Remote Sensing Lab (MRSLab), Indian Institute of Technology Bombay, Mumbai, India; [c]C-CORE and Department of Electrical and Computer Engineering, Memorial University of Newfoundland, St. John's, Newfoundland, Canada

ABSTRACT

The RADARSAT Constellation Mission (RCM) Compact Polarimetry (CP) data has become a key asset in crop mapping and monitoring for diverse agricultural landscapes. This study utilizes the unique capabilities of the RCM CP data for crop mapping. It performs a detailed comparison between single-date and multi-date classification to underscore the prowess of multi-temporal CP data in crop mapping. The novelty of our approach is in the thorough investigation of real CP data, a significant advancement from previous studies that mainly relied on simulated CP data. The CP data used in this study were acquired on July 1, July 30, and August 27, 2021, over southern Quebec, Canada, including soy, corn, hay, and cereal classes. Various features were extracted from the CP data, and the Random Forest classifier was utilized for crop mapping. The experimental results demonstrated the superiority of multi-temporal CP data for crop classification. The Overall Accuracy (OA) for single-date classifications on July 1, July 30, and August 27 were 61.10%, 75.00%, and 86.45%, respectively. In contrast, the multi-date analysis showed a marked increase in OA (91.20%). This substantial improvement underscores the significant benefit of incorporating multi-date CP data, which delivers a robust and precise framework for crop mapping.

RÉSUMÉ

Les données radar à synthèse d'ouverture en mode polarimétrie compacte (PC) de la Mission Constellation RADARSAT (MCR) sont devenues un atout majeur pour la cartographie et la. surveillance des cultures dans divers paysages agricoles. Cette étude utilise les capacités uniques des données P C de la mission RCM pour la cartographie des cultures. Elle effectue une comparaison détaillée entre la classification à une date et la classification à plusieurs dates pour souligner la petinance des données PC multitemporelles dans la cartographie des cultures. La nouveauté de notre approche réside dans l'évaluation approfondi des données CP réelles, ce qui constitue une avancée significative par rapport aux études précédentes qui s'appuyaient principalement sur des données PC simulées. Les données de PC utilisées dans cette étude ont été acquises le 1er juillet, le 30 juillet et le 27 août 2021, dans une region au sud du Québec, Canada, et comprennent des classes de soja, de maïs, de foin et de céréales. Diverses caractéristiques ont été extraites des données P C, et le classificateur Forêt des arbres aléatoires (Random Forest) a été utilisé pour la cartographie des cultures. Les résultats expérimentaux ont démontré la supériorité des données PC multitemporelles pour la classification des cultures. La précision globale (Overaal Accuracy: OA) pour les classifications à une seule date, le 1er juillet, le 30 juillet et le 27 août, était respectivement de 61,10 %, 75,00 % et 86,45 %. En revanche, l'analyse multi-dates a montré une nette augmentation de l'OA (91,20 %). Cette amélioration substantielle souligne l'avantage significatif de l'incorporation de données P C multi-dates, qui fournit un cadre robuste et précis pour la cartographie des cultures.

CONTACT Ramin Farhadiani ✉ ramin.farhadiani@inrs.ca
*These authors contributed equally to this work.

Introduction

Agricultural monitoring is a cornerstone in assessing crop health and yields, which are pivotal in the agricultural landscape (Omia et al. 2023; Wu et al. 2022). The primary objective of monitoring croplands is to streamline and enhance the profitability of farming practices. By facilitating in-depth analysis and supplying crucial information about the status of agricultural products, this process becomes an invaluable resource for analysts and decision-makers alike. While traditional monitoring methods may rely on human labor, the advent of crop monitoring through satellite Remote Sensing technology offers a reliable alternative to labor-intensive fieldwork. The benefits extend beyond the capabilities of the naked human eye, as satellite-based systems provide a comprehensive and real-time view of vast agricultural areas.

Various studies have comprehensively utilized optical satellite data for cropland monitoring (Yang et al. 2020; Kobayashi et al. 2020). However, it is crucial to acknowledge optical Remote Sensing's limitations, i.e., its sensitivity to severe weather conditions and impracticality in areas obscured by clouds or during nighttime observations. To overcome these challenges, the integration of Radar Remote Sensing, specifically Synthetic Aperture Radar (SAR), has emerged as a viable alternative (Shang et al. 2022; Sishodia et al. 2020).

One commonly accepted method of categorizing SAR data is by its polarization configurations, which include Single Polarized (SP), Dual Polarized (DP), and Full Polarimetric (FP) modes (Mahdianpari et al. 2019). Different configurations of SAR sensors provide varying levels of information content. The ability to distinguish between different crop types using SAR sensors is affected by the specific characteristics of the sensors. In this regard, DP SAR has been shown to outperform SP SAR, and FP SAR, in turn, typically surpasses DP SAR in precision (Mahdianpari et al. 2019).

However, the advantages of FP SAR systems come with significant drawbacks. A notable limitation of FP SAR systems is the doubled Pulse Repetition Frequency (PRF) requirement compared to SP or DP SAR systems (Charbonneau et al. 2010). This increase in PRF results in a 50% reduction in coverage width, impacting satellite coverage and increasing revisit times (Mahdianpari et al. 2019; Charbonneau et al. 2010). This constraint limits the practical application of FP SAR for operational tasks over extensive geographical areas.

While DP SAR partially addresses some of these issues, such as a smaller swath width, it still faces challenges, notably the inability to maintain a relative phase between co- and cross-polarization channels (Dubois-Fernandez et al. 2008). Compact Polarimetry (CP) SAR systems present a potential solution by emitting one polarization and receiving two coherent polarizations. Notably, CP systems can acquire data with a swath width twice as large, addressing some limitations associated with coverage width and revisit times (Charbonneau et al. 2010). Additionally, CP systems preserve the relative phase between polarization channels, enhancing their utility in addressing the challenges faced by both DP and FP SAR systems.

RADARSAT Constellation Mission (RCM) was successfully launched on June 12, 2019 using the SpaceX Falcon 9 rocket. This launch marked Canada's latest step in Remote Sensing with SAR. RCM, Canada's newest Earth-watching SAR satellite series, includes a quick 4-day return visit, a special CP mode, and broad area monitoring using ScanSAR mode (Thompson 2010; Canadian Space Agency 2023). The C-band RCM satellites orbit at an average height of 593 km and are spaced 120° apart. Each satellite revisits every 12 days, ensuring a 4-day revisit cycle together.

A distinct feature of RCM compared to its predecessor, FP RADARSAT-2, is the introduction of the CP mode (Canadian Space Agency 2023). In the RCM system, CP utilizes a right-handed circular (RHC) transmission while recording the H and V polarizations coherently upon their return, termed circular-transmit and linear-receive (CL) (Dingle Robertson et al. 2022). A circular transmission waveform occurs when the H and V polarizations operate together but with a 90° phase difference (Raney 2007). As previously mentioned, the coverage width of FP SAR systems is halved due to the increased PRF (Charbonneau et al. 2010). For instance, in the RCM system, the FP mode typically covers an area of around 20 km in width. Even though this mode provides a comprehensive dataset, its limited coverage is unsuitable for national mapping. Alternatively, when developing the RCM, CP was introduced as a potential answer for those needing extensive coverage while preserving the depth of polarization data (Raney 2007).

Nearly all the published research regarding agricultural land monitoring has been conducted on the simulated CP data due to the limited access to the actual CP data. Hence, researchers simulated the CP data from the FP SAR data. Charbonneau et al. (2010) researched crop classification based on the simulated CP data in 2010. Four FP RADARSAT-2 images obtained over eastern Ontario, Canada, and during the growing season were used for simulation. Utilizing

the Decision Tree (DT) classifier and based on Stokes parameters extracted from the simulated CP images, the classification was done, and 91% accuracy was reached, which was higher than the classification using dual-polarization, i.e., HH + VV and HH + HV and Freeman-Durden decomposition parameters.

Brisco et al. (2013) also used DP, FP, and simulated CP SAR data. The data used in this research was obtained from four RADARSAT-2 images in China. The Support Vector Machine (SVM) classifier was employed for classification. Using Stokes parameters and m-delta decomposition, the authors showed that simulated CP data with an accuracy of around 95% was more effective than DP data but was lower than FP data. Similarly, another research was done in the Leizhou Peninsula, southern China, by Xie et al. (2015). A time-series TerraSAR-X data was used to simulate the CP data. The classification was done using a proposed unified classification framework. They compared the results with FP and coherent HH/VV modes and showed that Overall Accuracy (OA) for data in the FP and coherent HH/VV modes was almost 95%, while it was around 91% for the CP data.

Three studies were conducted based on simulated CP data using RISAT-1 data in India. Uppala et al. used single-date RISAT-1 data for maize crop discrimination (Uppala et al. 2016). The study area was located in Vemuru Mandal, Guntur district of Andhra Pradesh, India, and the Parallelepiped Minimum Distance classifier was adopted for the classification task. The results were also compared with Resourcesat-2 LISS-III optical data, which was classified using the Maximum Likelihood classifier. The OA of LISS-III and RISAR-1 were 92% and 89%, respectively. In 2017, Chirakkal et al. simulated CP data based on RISAT-1, obtained over the Hisar district of Haryana and Junagadh district of Gujrat, India, and employed the Maximum Likelihood classifier (Chirakkal et al. 2017). In this study, the authors showed that the classification based on the CP m-chi decomposition generally results in better crop separability. In 2018 (Dasari and Lokam 2018), the RISAT-1 datasets (simulated CP and DP data) obtained over the northern part of Telangana State in the Ghanpur Village, district of Warangal, India, were used by Dasari et al. for land cover classification using SVM classifier and based on Radial Basis Function (RBF), Polynomial with degree 2 and linear kernels. The authors showed that SVM with RBF kernel has the highest OA of 92.34% and 76.83% for simulated CP and DP RISAT-1 data.

Pixel-based and object-based Random Forest (RF) classification was used by Mahdianpari et al. (2019) for mid-season classification. The CP images were simulated using four RADARSAT-2 images obtained over agricultural land in Manitoba, Canada. Different features derived from the FP, simulated DP, and CP SAR images were employed as the classifier's input. 88.2%, 82.1%, and 77.3% accuracy were reported using the object-based RF classifier for the FP, CP, and DP SAR images, respectively.

In 2019, Robertson et al. (2019) employed simulated CP data based on three RADARSAT-2 images acquired over southern Manitoba, Canada. Ten CP features were extracted for each image, and the RF classifier was used to classify this data stack. Some classes, such as canola and soybeans, had higher accuracies (canola of 71% and 72% and soybean of 72% and 78%, respectively), although the preliminary OA was poor (fewer than 65%).

In contrast to the previous research studies conducted on simulated CP data, Dingle Robertson et al. employed real RCM CP data in 2022 (Dingle Robertson et al. 2022). Using the RF classifier, RCM CP images acquired over agricultural land in Kenaston within the province of Saskatchewan, Canada, were used for the crop mapping. An OA of 95% was achieved, about 2% lower than a classification using optical imagery with post-processing filtering.

Jafarzadeh et al. (2024) recently used RCM CP SAR data from southern Quebec in Canada for crop monitoring. In their study, they introduced three new analytical descriptors: the compact-polarimetric SAR signature (CPS), differential CPS (DCPS), and the geodesic distance (GD) between signatures to analyze crop-type scattering behaviors. Furthermore, the study extensively examined CP SAR data, extracting various parameters for crop classification using the RF classifier. Multiple classification runs were conducted across two scenarios, testing different combinations of CP inputs. The multi-date crop mapping approach achieved an impressive OA of 89.71%, demonstrating the effectiveness of integrating features from CP data.

Table 1 summarizes the research conducted on CP data for crop mapping, using either simulated or real data. Notably, the studies conducted before the launch of the RCM satellite in 2019 utilized simulated data to develop and test various classification algorithms, ranging from DT to more complex RF methods. Simulated CP data would help understand the potential of CP data for various classification tasks when the real data is unavailable. However, a pronounced research gap is evident in using real CP data, with only two studies conducted by Dingle Robertson et al. in 2022 and Jafarzadeh et al. in 2024 using real RCM CP data addressing this domain. The reliance on simulated CP data could pose limitations, as it may not fully capture the properties in real-world scenarios.

Table 1. Summary of research conducted on simulated and real CP data.

CP data type	Authors	Year	Data	Study area	Classifier
Simulated	Charbonneau et al.	2010	RADARSAT-2	Ontario, Canada	Decision Tree
	Brisco et al.	2013	RADARSAT-2	China	Support Vector Machine
	Xie et al.	2015	TerraSAR-X	Leizhou Peninsula, China	A Unified Framework
	Uppala et al.	2016	RISAT-1	Vemuru Mandal, India	Parallelepiped Minimum Distance
	Chirakkal et al.	2017	RISAT-1	Hisar district of Haryana, India	Maximum Likelihood
	Easari et al.	2018	RISAT-1	Ghanpur Village, India	Support Vector Machine
	Dingle Robertson et al.	2019	RADARSAT-2	Manitoba, Canada	Random Forest
	Mahdianpari et al.	2019	RADARSAT-2	Manitoba, Canada	Pixel- and Object-based Random Forest
Real	Dingle Robertson et al.	2022	RCM Compact Polarimetry	Saskatchewan, Canada	Random Forest
	Jafarzadeh et al.	2024	RCM Compact Polarimetry	Quebec, Canada	Random Forest

The performance of classification algorithms validated on simulated CP data may not necessarily translate to similar effectiveness when applied to real CP data. This gap underscores the need for further empirical studies employing real CP data to validate their robustness and reliability for practical applications in cropland monitoring. Such research would significantly contribute to the existing body of knowledge by providing a more accurate assessment of the capabilities and limitations of CP SAR data in real-world agricultural settings. Thus, the main objective of this study is to evaluate the effectiveness of RCM CP data for crop mapping. The research will specifically focus on two key questions. Firstly, we will evaluate how integrating multi-date CP data influences classification accuracy compared to single-date CP data. Secondly, we will identify the most critical CP features that contribute to the precision of crop classification.

Compact polarimetry: principles and features

At the level of an individual pixel in its single-look complex form, the system measures a representation of the complex scattering matrix (Cloude et al. 2012),

$$\begin{bmatrix} E_{CH} \\ E_{CV} \end{bmatrix} = \frac{1}{\sqrt{2}} \begin{bmatrix} S_{HH} & S_{HV} \\ S_{VH} & S_{VV} \end{bmatrix} \begin{bmatrix} 1 \\ \pm i \end{bmatrix} = \frac{1}{\sqrt{2}} \begin{bmatrix} S_{HH} \pm iS_{HV} \\ S_{VH} \pm iS_{VV} \end{bmatrix} \quad (1)$$

where the symbol + illustrates the left-hand circular (LHC) transmission and the − shows the right-hand circular (RHC) transmission (Cloude and Pottier 1996). For CP RHC polarization, the − sign must be adopted. In contrast to the FP modes, which utilize a 3×3 covariance matrix, the scattering information in CP mode is represented using a 2×2 covariance matrix C2 (Dey et al. 2021):

$$C2 = \begin{bmatrix} \left\langle \left| E_{RH} \right|^2 \right\rangle & \left\langle E_{RH} E_{RV}^* \right\rangle \\ \left\langle E_{RV} E_{RH}^* \right\rangle & \left\langle \left| E_{RV} \right|^2 \right\rangle \end{bmatrix} \quad (2)$$

where R means the signal is transmitted in the RHC form, and H and V represent the received backscattered signal in horizontal or vertical polarization. The diagonal elements of the C2 matrix are equivalent to the backscattered coefficients in RH and RV polarization channels. The off-diagonal elements of the C2 matrix represent the complex correlation of backscattered information between RH and RV polarization channels.

Within the specialized domain of compact polarimetry, a collection of distinct features that are indispensable for advanced data interpretation has been developed. These features enable a complex understanding of the data, facilitating the extraction of detailed insights from information gathered through this type of satellite imagery. In the rest of this section, we will briefly describe each CP decomposition.

- ***Stokes parameters:*** The Stokes parameters, containing four components, derived from the C2 matrix, define the polarization state of a partially polarized electromagnetic (EM) field (Raney et al. 2021). The first Stokes parameter (S_0) demonstrates the total intensity of the radar's backscatter signal, encompassing both polarized and unpolarized components, which is the sum of the powers of the two received waves with orthogonal polarizations. The three other parameters (S_1, S_2, and S_3) indicate the characteristics of the EM field's polarized portion (Dingle Robertson et al. 2022). Specifically, S_1 shows the dominance of linear horizontal polarization light over the vertical one. S_2 illustrates the predominance of linear +45° polarized light over linear −45° polarized light (Collett 2005). S_3 depicts the dominance of right-handed circular polarization compared to left-handed circular polarization (Collett 2005). The determination of S_1 stems from the difference between the powers

of the received channels. Meanwhile, S_2 and S_3 are extracted from the complex cross-products of the received EM waves (Raney 2006, 2019).

- **Stokes child parameters:** It is possible to derive other parameters referred to as the Stokes child parameters from the Stokes vector, which help extract more specific information from the Stokes parameters and have demonstrated their value in assisting image feature analysis (Mahdianpari et al. 2019). The first Stokes child parameter is the degree of polarization (m), where the extreme values, either 0 or 1, correspond to an EM field that is entirely unpolarized or completely polarized, respectively (Raney et al. 2021). The degree of depolarization, i.e., $1 - m$, points to randomly polarized backscatter, generally originating from materials nearly transparent to radar signals (Raney et al. 2012).

The Stokes parameters, i.e., S_1, S_2, and S_3, can be represented through the Poincaré variables (Brisco et al. 2020), as demonstrated in Figure 1, where χ and δ denote the ellipticity and the orientation of the polarization ellipse's long axis, and m represents the degree of polarization (Dingle Robertson et al. 2022). These two parameters, i.e., the degree of circularity (χ) and relative phase angle (δ), can be considered Stokes child parameters.

Another set of parameters that can be computed based on the Stokes parameters is the Circular Polarization Ratio (μ_c) and degree of linear
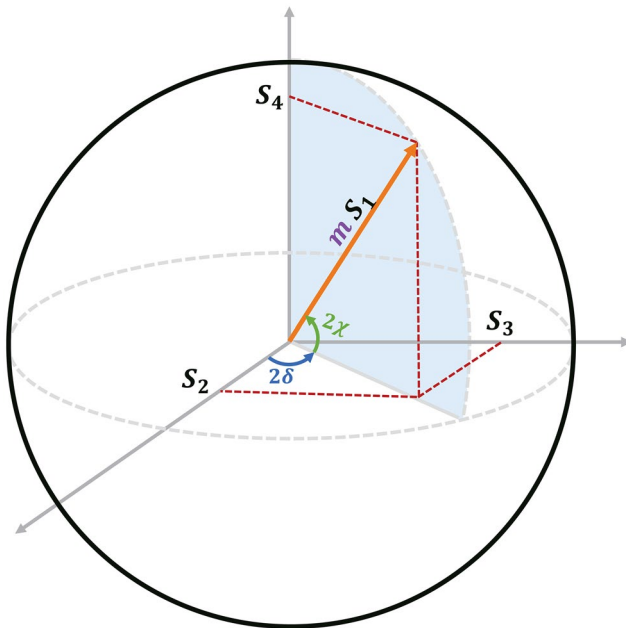

Figure 1. The geometrical relationship between Stokes and Poincaré parameters (Brisco et al. 2020).

polarization (m_L) in the backscattered field. It should be noted that μ_c is less than unity for most single- or odd-bound backscatter situations, while it is greater than unity in other cases. Another Stokes child parameter is α_s (i.e., the ellipticity of the compact scattered wave (Mahdianpari et al. 2019), which is closely related to the ellipticity of the compact scattered wave (Cloude 2009; Raney 2006).

- **m-chi and m-delta decompositions:** The m-chi decomposition (Raney et al. 2012) can be computed based on the first Stokes parameter (S_0), degree of circularity (χ), and degree of polarization (m), indicating single-bounce ($m_{\chi_{Blue}}$), double-bounce ($m_{\chi_{Red}}$), and randomly polarized constituent (or volume) backscattering ($m_{\chi_{Green}}$), respectively. Like the m-chi decomposition, the m-delta decomposition (Charbonneau et al. 2010) utilizes the first Stokes component (S_0) and the degree of polarization (m), but it uses the relative phase angle (δ), where $m_{\delta_{Blue}}$ can be related to the surface scattering, while the $m_{\delta_{Red}}$ and $m_{\delta_{Green}}$ illustrate the double-bounce and volume scattering, respectively.

- **H/A/Alpha:** Like the FP H/A/Alpha decomposition, in the case of CP data, H/A/Alpha decomposition contains three components, i.e., Entropy (H), Anisotropy (A), and Alpha ($\bar{\alpha}$), computing based on the eigenvectors and eigenvalues (Zhang et al. 2014). The Entropy measures the scattering randomness, with values between 0 and 1, which shifts from completely polarized to entirely random scattering. If H = 0, it indicates isotropic scattering under a completely polarized state. In contrast, H = 1 means anisotropic scattering with complete randomness, rendering polarization information unattainable. The Anisotropy complements Entropy and becomes less informative when H is exceptionally high or low. The Alpha, which varies from 0° to 90°, indicates different physical scattering mechanisms. Specifically, $\bar{\alpha} = 0°$ indicates surface scattering, and $\bar{\alpha} = 90°$ is related to dihedral or helix scattering. As for $0° < \bar{\alpha} < 45°$ and $45° < \bar{\alpha} < 90°$, it demonstrates dipole scattering and dihedral scattering, respectively (Lee and Pottier 2017; Van Beijma et al. 2014; You et al. 2014).

- **RVOG-based decomposition:** Random Volume Over Ground (RVOG) based CP decomposition has three components. It can be computed based on the first element of the Stokes vector (S_0), degree of polarization (m), and ellipticity of the

compact scattered wave (α_s) (Cloude et al. 2012), containing three components: surface scattering component (P_{Blue}), dihedral component power (P_{Red}), and volume power (P_{Green}).

- **Dey et al. decomposition:** The CP decomposition proposed by Dey et al. (2021) contains four components: target characterization parameter (θ_{CP}), as well as $P_{\text{Blue}}^{\text{CP}}, P_{\text{Red}}^{\text{CP}}$, and $P_{\text{Green}}^{\text{CP}}$, which are related to the surface, double-bounce, and volume scattering. It should be noted that θ_{CP} can take on any value between -45° and 45°, including the endpoints.

- **Other decompositions:** Some CP features are not categorized as either Stokes child parameters or decompositions. Among them is the conformity coefficient (μ), which is Faraday Rotation independent, ranging from -1 to 1. Considering the reflection symmetry assumption for the distributed targets, when positive μ values are near 1, surface scattering is predominant; when negative μ values approach -1, double-bounce scattering takes over; and for middle-range μ values, volume scattering is the most prominent (Truong-Loi et al. 2009).

In total, 90 CP features were extracted from the multi-temporal CP SAR data (30 CP features for each date) and used for further analysis. The mathematical formulas for computing the discussed CP features are summarized in Table 2. It should be noted that in the H/A/Alpha decomposition, by applying eigen decomposition on the C2 covariance matrix, it can be expressed as a weighted sum of two matrices, i.e., C2]$_1$ and C2]$_2$. These matrices correspond to the two distinct scattering mechanisms occurring at the pixel level (Ioannidou et al. 2022):

$$\text{C2} = \begin{bmatrix} U \end{bmatrix} \begin{bmatrix} \lambda_1 & 0 \\ 0 & \lambda_2 \end{bmatrix} \begin{bmatrix} U \end{bmatrix}^T = \lambda_1 \vec{u}_1 \vec{u}_1^T + \lambda_2 \vec{u}_2 \vec{u}_2^T = \lambda_1 \begin{bmatrix} \text{C2} \end{bmatrix}_1 + \lambda_2 \begin{bmatrix} \text{C2} \end{bmatrix}_2$$

$$(3)$$

and

$$\begin{bmatrix} U \end{bmatrix} = \begin{bmatrix} U_{11} & U_{12} \\ U_{21} & U_{22} \end{bmatrix} = \begin{bmatrix} \vec{u}_1 & \vec{u}_2 \end{bmatrix} \tag{4}$$

where $[U]$ demonstrates the orthogonal, unitary matrix, as well as $\vec{u}_i$ and λ_i ($i=1,2$) are the eigenvector and the corresponding eigenvalue. The eigenvector $\vec{u}_i$ can also be parametrized using two angular variables,

i.e., scattering mechanism (α_i) and phase angle (δ_i) as follows (Ioannidou et al. 2022):

$$\vec{u}_i = \begin{bmatrix} \cos\alpha_i & \sin\alpha_i e^{j\delta_i} \end{bmatrix}^T, \quad i=1,2 \tag{5}$$

where p_i and α_i can be computed as (Zhang et al. 2014):

$$p_i = \frac{\lambda_i}{\lambda_1 + \lambda_2}, \quad i=1,2 \tag{6}$$

$$\alpha_i = \cos^{-1}\left(|u_{1i}|\right) \tag{7}$$

Furthermore, in the Dey et al. decomposition, m_{CP} (2D Barakat degree of polarization) can be computed as:

$$m_{\text{CP}} = \sqrt{1 - \frac{4|\text{C2}|}{(\text{Trace}(\text{C2}))^2}} \tag{8}$$

Additionally, OC and SC can be computed based on the Stokes vector elements as follows:

$$\text{OC} = \frac{S_0 + S_3}{2} \tag{9}$$

$$\text{SC} = \frac{S_0 - S_3}{2} \tag{10}$$

Methodology

Study area

The study area, highlighted by a red rectangle in Figure 2, covers an agricultural region in southern Quebec, Canada, and contains various crop types, such as soy, hay, oats, wheat, barley, corn, etc. The study area is geographically defined within the coordinates approximately bounded by 46° 2′N to the north, 45° 52′N to the south, 73° 7′W to the west, and 72° 46′W to the east.

CP multitemporal data processing

We utilized three ascending Single Look Complex (SLC) RCM CP images for crop monitoring between July 1 and August 27, 2021. These images were acquired with a spatial resolution of 5 m using the StripMap beam mode. Table 3 presents the details of this multitemporal CP data employed in this paper. Figure 3 also illustrates the RGB images of these three CP data.

Table 2. Polarimetric features extracted from compact polarimetry SAR data.

Feature name	Description	Formula	References
Intensity	Intensity values of $C2$ matrix	$\lvert E_{RH} \rvert^2, \lvert E_{RV} \rvert^2$	–
Stokes vector parameters	The first element	$S_0 = \lvert E_{RH} \rvert^2 + \lvert E_{RV} \rvert^2$	Raney et al. 2012
	The second element	$S_1 = \lvert E_{RH} \rvert^2 - \lvert E_{RV} \rvert^2$	
	The third element	$S_2 = 2\mathrm{Re}(E_{RH} E_{RV}^*)$	
	The fourth element	$S_3 = -2\mathrm{Im}(E_{RH} E_{RV}^*)$	
Stokes child parameters	Degree of polarization	$m = \dfrac{\sqrt{S_1^2 + S_2^2 + S_3^2}}{S_0}$	Raney et al. 2012
	Degree of depolarization	$1 - m$	Raney et al. 2012
	Degree of circularity	$\sin 2\chi = -\dfrac{S_3}{m S_0}$	Raney et al. 2012
	Relative phase	$\delta = \tan^{-1}\left(\dfrac{S_3}{S_2}\right)$	Charbonneau et al. 2010
	Circular polarization ratio	$\mu_c = \dfrac{S_0 + S_3}{S_0 - S_3}$	Charbonneau et al. 2010
	Degree of linear polarization	$m_L = \dfrac{\sqrt{S_1^2 + S_2^2}}{S_0}$	Raney et al. 2021
	Alphas	$\alpha_s = \dfrac{1}{2}\tan^{-1}\left(\dfrac{\sqrt{S_1^2 + S_2^2}}{S_3}\right)$	Cloude et al. 2012
CP decompositions	m-chi	$m_{\chi_{Blue}} = \sqrt{S_0 m \dfrac{(1 - \sin 2\chi)}{2}}$ $m_{\chi_{Red}} = \sqrt{S_0 m \dfrac{(1 + \sin 2\chi)}{2}}$ $m_{\chi_{Green}} = \sqrt{S_0 (1 - m)}$	Raney et al. 2012
	m-delta	$m_{\delta_{Blue}} = \sqrt{S_0 m \dfrac{(1 + \sin(\delta))}{2}}$ $m_{\delta_{Red}} = \sqrt{S_0 m \dfrac{(1 - \sin(\delta))}{2}}$ $m_{\delta_{Green}} = \sqrt{S_0 (1 - m)}$	Charbonneau et al. 2010
	H/A/Alpha	$H = -p_1 \log_2 p_1 - p_2 \log_2 p_2$ $A = \dfrac{\lambda_1 - \lambda_2}{\lambda_1 + \lambda_2}$ $\bar{\alpha} = p_1 \alpha_1 + p_2 \alpha_2$	Zhang et al. 2014
	RVOG-based	$P_{Blue} = \dfrac{1}{2} S_0 m (1 + \cos 2\alpha_s)$ $P_{Red} = \dfrac{1}{2} S_0 m (1 - \cos 2\alpha_s)$ $P_{Green} = S_0 (1 - m)$	Charbonneau et al. 2010

Table 2. Continued.

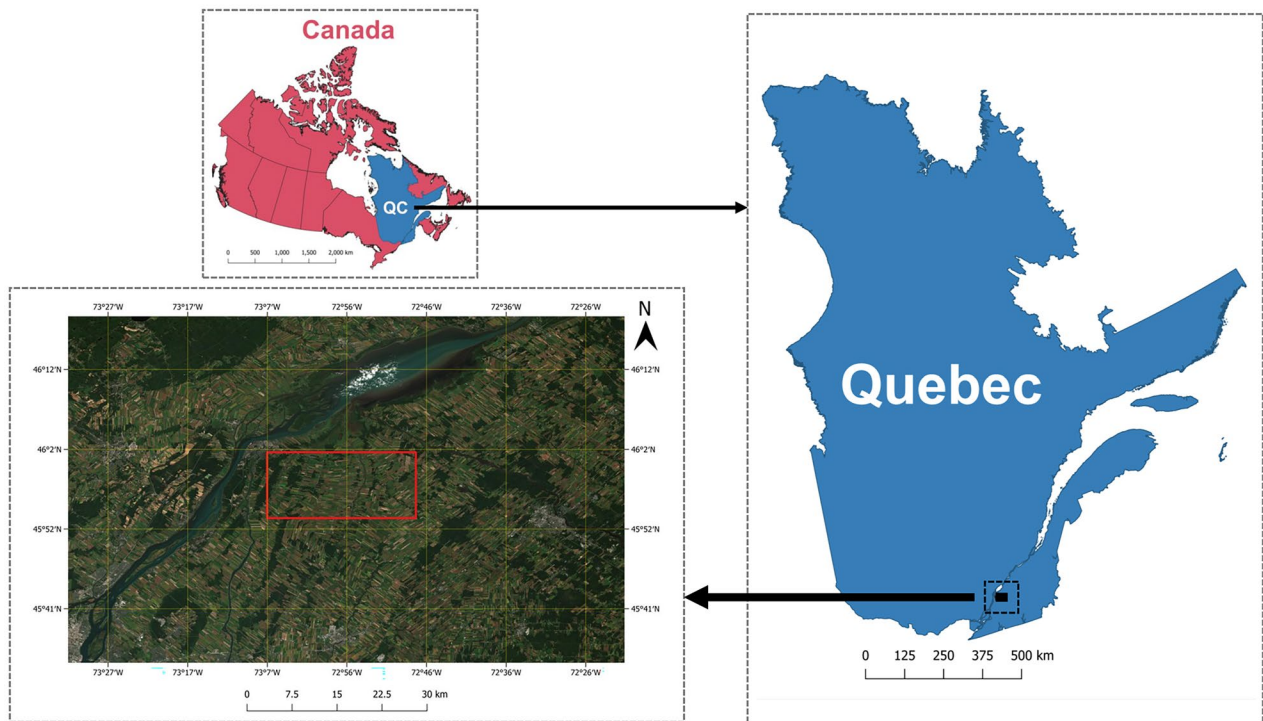| Feature name	Description	Formula	References
	Dey et al.	$P_{\text{Blue}}^{CP} = \dfrac{m_{CP} S_0}{2}(1+\sin 2\theta_{CP})$	Dey et al. 2021
		$P_{\text{Red}}^{CP} = \dfrac{m_{CP} S_0}{2}(1-\sin 2\theta_{CP})$	
		$P_{\text{Green}}^{CP} = S_0(1-m_{CP})$	
		$\tan\theta_{CP} = \dfrac{m_{CP} S_0(\text{OC}-\text{SC})}{\text{OC}\times\text{SC}+m_{CP}^2 S_0^2}$	
Others	Conformity coefficient	$\mu = \dfrac{2\text{Im}\left\langle S_{RH} S_{RV}^* \right\rangle}{\left\langle S_{RH} S_{RH}^* \right\rangle + \left\langle S_{RV} S_{RV}^* \right\rangle}$	Truong-Loi et al. 2009

Figure 2. Study area location: southern Quebec, Canada.

Table 3. Multi-temporal CP data description.

#	Satellite	Acquisition date	Orbit pass	Beam mode	Swath width	Polarization, resolution
1	RCM1	July 1, 2021	Asc.	High Res. StripMap	30 km	RH and RV, 5 m
2	RCM2	July 30, 2021				
3	RCM3	August 27, 2021				

Preprocessing of CP SAR data is essential for crop mapping and is crucial for precise land cover classification. In our research, we preprocessed the CP images utilizing the freely available open-source SNAP software (European Space Agency 2024). The preprocessing workflow is illustrated in Figure 4. Initially, calibration was performed on the raw data, i.e., SLC data (RH and RV), to convert them into sigma-naught backscattering coefficients. Subsequently, multilooking was performed using a 2×2 window size in the azimuth and range direction. While multilooking reduces the speckle, it also leads to a reduction in spatial resolution. The
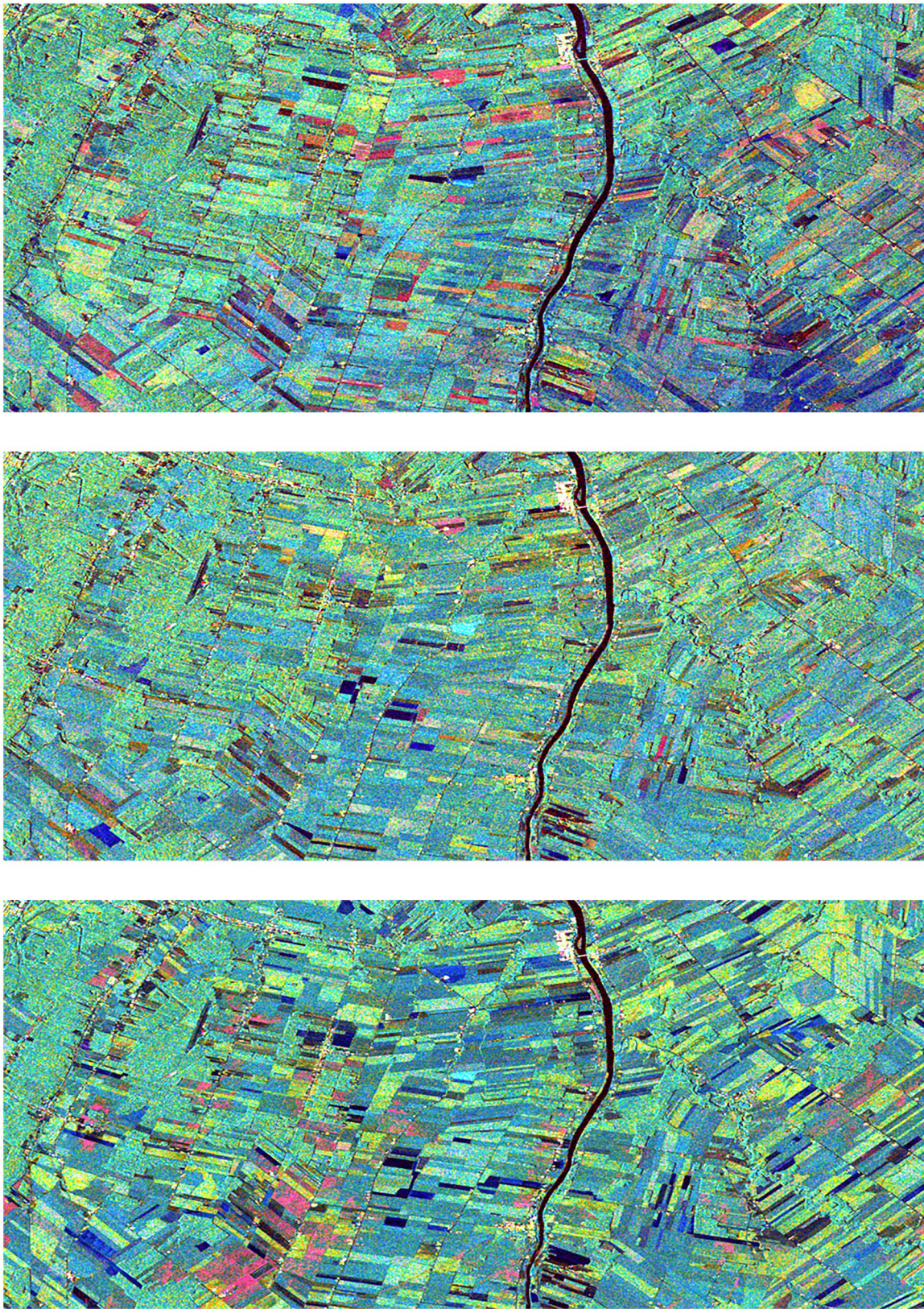
Figure 3. RGB images based on m-chi decomposition, from top to down, July 1, July 30, and August 27, respectively.

next step involved generating the 2×2 C2 covariance matrix and applying a 5×5 boxcar filter to mitigate the speckle further. Terrain correction was then applied to the elements of the C2 matrix. Next, all three CP images were subset and masked to achieve the area of interest. Next, the preprocessed datasets were
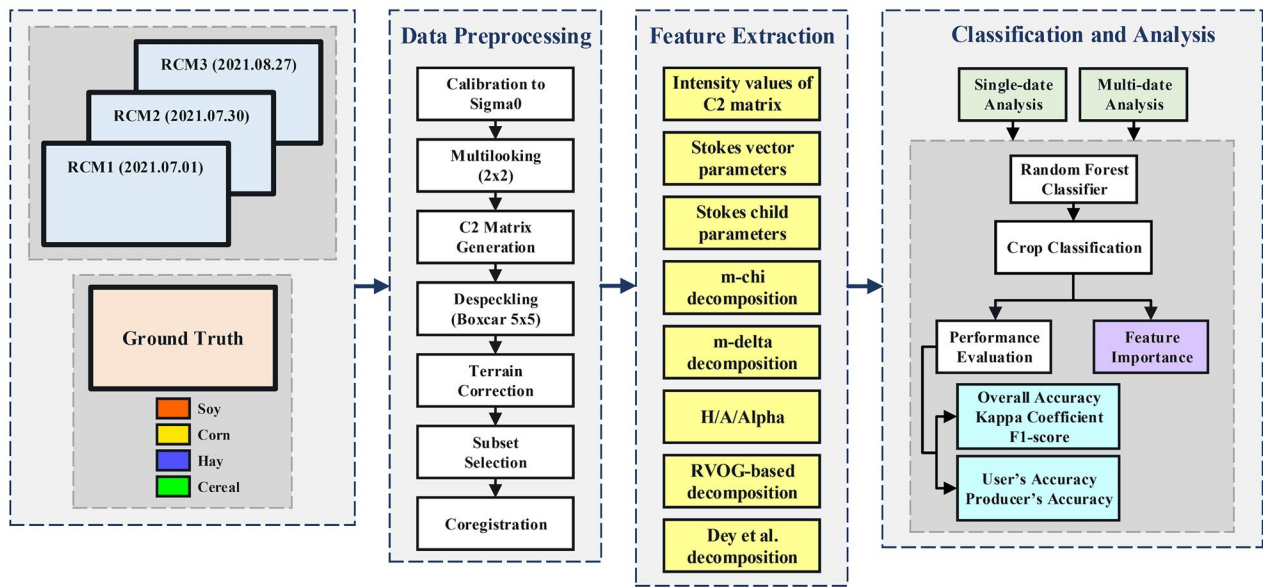
Figure 4. Workflow of the CP data preprocessing.

categorized and stacked together. The reference image was 1 July in coregistration, and the rest were considered secondary images. Various features were then extracted from the C2 matrix, listed in Figure 4 and Table 2. Finally, the preprocessed CP multitemporal stack was used as an input for the classifier.

Reference data

Collecting information as the ground truth covering large areas can be challenging. On-the-ground data collection can be expensive, especially involving specialized equipment, significant travel, or a large team of surveyors to collect first-hand and high-fidelity information. A practical alternative is to utilize established official products, such as the BDPPAD (Base de données des parcelles et productions agricoles déclarées) provided by La Financière agricole du Québec (FADQ) as the ground truth data. BDPPAD is a database consisting of vector-format polygons representing the contours of crop fields. These field boundaries have been associated with the client files of FADQ since 2003 (Government and Municipalities of Québec 2023; La Financière agricole du Québec 2023). Initially, the database was focused on generalized crops, but over time, it evolved to encompass individual parcels and multiple crops per parcel. The data now includes geospatial information on agricultural parcels and data on declared agricultural productions, not just crop-related data. It is stored in a Shapefile format with geographic coordinates in the North American Datum 83 (NAD 83) coordinate system. In this study, this data was adopted as the ground truth.

It should be noted that the reference data comprised various classes. However, some specific classes were excluded due to limited reference samples and minimal spatial coverage. Classes with similar crop yields were amalgamated into a single class to simplify the analysis, resulting in a four-class ground truth dataset. Hence, the focus is on the most relevant classes, optimizing processing efficiency.

Figure 5(a) illustrates four main crop types in the study area: soy, corn, hay, and cereal. The total pixel count for each class is also presented in Table 4. As shown in Figure 5 and Table 4, the soy and corn classes dominate the two other classes, leading to imbalanced ground truth data. For the classification task, we split the data into training (70%), validation (15%), and test (15%) sets using stratified splitting. This splitting method is particularly indispensable when using imbalanced datasets, where one or more classes are present in much higher numbers than others. Stratified splitting preserves the original class distribution across the subsets, thereby mitigating the introduction of bias during the model training and evaluation phases. Stratified splitting is essential in scenarios, such as crop classification, where an imbalanced distribution could potentially skew the model's leaning toward the dominant classes, adversely affecting the model's generalization capability. Moreover, in the hyperparameters tuning phase, employing a validation set derived through stratified splitting provides a more accurate reflection of the model's performance across all classes, thus facilitating a more informed and effective selection of hyperparameters.
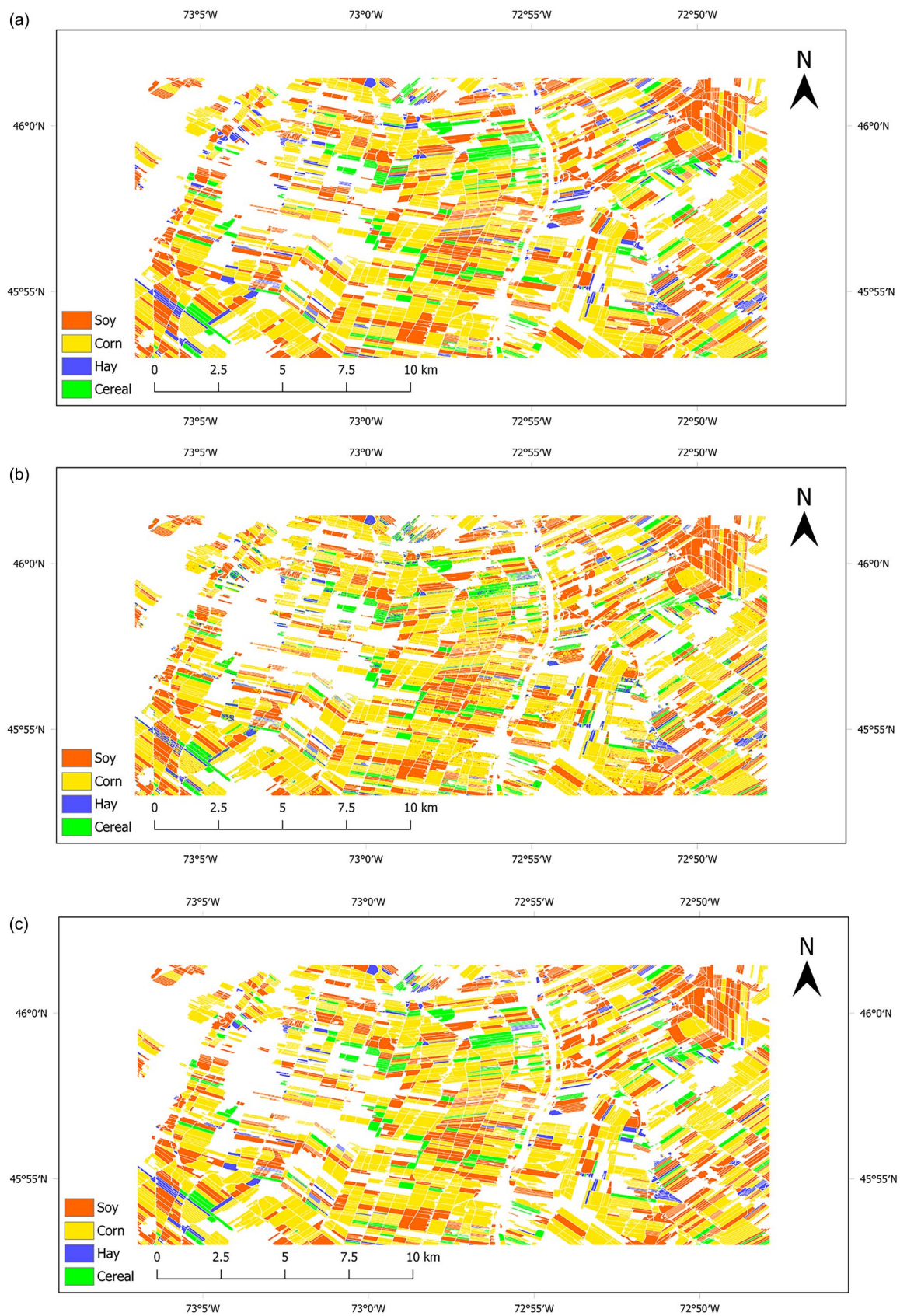
Figure 5. (a) Ground truth, (b) the final crop map, and (c) postprocessed crop map.

Table 4. Number of train, validation, and test pixels for each crop.

Class	Train [70%]	Validation [15%]	Test [15%]	Total
Soy	1,125,448	241,168	241,167	1,607,783
Corn	1,924,920	412,484	412,483	2,749,887
Hay	156,689	33,576	33,577	223,842
Cereal	301,130	64,527	64,528	430,185
Total	3,508,187	751,755	751,755	5,011,697

Table 5. Grid-search parameters used in the RF model.

Parameters	Description	Grid search values
n_estimators	Number of trees in the forest	5, 10, 25, **50**, 100
max_depth	Maximum depth of the trees	2, 3, 5, 8, **10**
min_samples_split	Minimum number of samples required to split an internal node	2, 3, 5, **10**
min_samples_leaf	Maximum number of samples required to be at a leaf node	1, 2, **3**, 5, 10

The bold values indicate the best-performing parameters.

Random Forest classifier

In the Remote Sensing community, the effectiveness and robustness of the RF classifier (Breiman 2001) have been widely accepted across a range of applications (Sheykhmousa et al. 2020), ranging from land use classification (Billah et al. 2023) to crop mapping (Orynbaikyzy et al. 2022). The RF classifier has various advantages over deep learning-based classifiers. The RF classifier does not require extensive computational resources, unlike deep learning models that often need powerful GPUs for training. They are much quicker to train and are suitable for tasks where interpretability is important since RF can provide insights into the importance of features. Additionally, RF classifiers are less prone to overfitting due to their ensemble nature. The RF model can also perform well with a smaller amount of data and require less hyperparameter tuning than deep learning models, which typically require large datasets and extensive training time to achieve high performance.

For the RF classification, the Scikit-learn module in Python is used in this research (Pedregosa et al. 2011). Regarding RF hyperparameter tuning, some parameters must be tuned, i.e., number of trees in the forest, maximum depth of the trees, minimum number of samples required to split an internal node, and maximum number of samples needed to be at a leaf node. For this purpose, the validation set was used to identify optimal hyperparameters of the RF classifier through grid search. The diverse parameters utilized in the grid search are presented in Table 5, with the best parameters indicated in bold. After tuning the optimal hyperparameters, the training and validation data are merged and used as the input data to train the RF model.

Experimental results

Figure 5(b) illustrates the final crop map derived from the classification of all 90 CP features discussed in section Compact polarimetry: principles and features. A post-classification refinement technique was also employed by assigning the most frequently occurring class within each polygon to the entire polygon to mitigate the salt-and-pepper noise typical of pixel-based classification and improve the thematic accuracy of the crop map. This majority voting approach harmonized the classification output and better represented the predominant land cover within each surveyed polygon. Figure 5(c) showed the refined crop map. The visual analysis of Figure 5 highlights the significant potential of utilizing multi-temporal CP data for generating a crop map, as evidenced by the striking resemblance between the classified image and the ground truth. However, by meticulously visually inspecting the classified image against the ground truth, it becomes evident that the classification algorithm has performed differently across various crop types. The soy and corn classes had a robust performance, as indicated by the strong visual correlation between the colors representing these crops in the ground truth and the classified images, suggesting a high level of accuracy in classifying these crop types. At the same time, there were discrepancies where hay and cereal classes were either confused with each other or with other crop types.

However, a quantitative assessment of the classification outcome is imperative to ensure a precise evaluation. For this purpose, several metrics were employed, including OA, the Kappa Coefficient, and the F1-score, as well as the Users' and Producers' accuracies (UA and PA, respectively). It should be noted that due to the imbalanced nature of the reference data that we used for the classification, relying solely on OA and Kappa Coefficient might be insufficient. The primary limitation of OA is that it can be misleading in the context of imbalanced datasets. If one class heavily outnumbers others, a classifier that always predicts this dominant class can still achieve high accuracy. While the Kappa Coefficient provides a more balanced measure than OA, it still has limitations. In certain situations, if one class has very few instances, the Kappa Coefficient might still not fully capture the model's inefficacy in identifying that class.

Table 6. OA, kappa coefficient, and F1-score for single-date and multi-date CP data.

Dates	OA	Kappa	F1-score
July 1	61.10%	0.41	66.06%
July 30	75.00%	0.55	73.91%
August 27	86.45%	0.76	85.51%
July 1 + July 30 + August 27	91.20%	0.85	91.04%

On the other hand, the F1-score becomes particularly important in the context of imbalanced data. It is a harmonic mean of precision (i.e., UA) and recall (i.e., PA). Therefore, even if a model performs well in precision but poorly in recall (or vice versa), the F1-score will reflect this imbalance, making the F1-score a more comprehensive metric to evaluate the performance of minority classes in imbalanced datasets.

Single-date versus multi-data CP classification

To illustrate the potential of multitemporal CP data for crop classification, we performed the RF classifier on multi-date CP data and individual single-date CP data from three distinct dates: July 1, July 30, and August 27. Table 6 presents the classification results, indicating the OA, Kappa coefficient, and F1-score values for both single-date and multi-date CP classification scenarios. Figure 6 also illustrates the corresponding confusion matrices resulting from the classification of single-date and multi-date CP data. From Table 6, it becomes evident that the multitemporal CP data offers superior classification performance compared to any of the single-date data sets. In fact, for all three single-dates, the classification outcomes were lower. On July 1, the OA stood at 67.10%, while the Kappa Coefficient was considerably lower, registering at 0.41. The F1-Score for this date was also 66.06%. By July 30, there was a marked improvement in OA, rising to 75.00%, while the Kappa Coefficient and F1-score increased to 0.55% and 73.91%, respectively. For August 27, the OA surged to an impressive 86.45%. The Kappa Coefficient also increased substantially to 0.76. The F1-Score for this date was even higher at 85.51%. When observing the multitemporal dataset, i.e., classification based on CP data obtained on July 1, July 30, and August 27
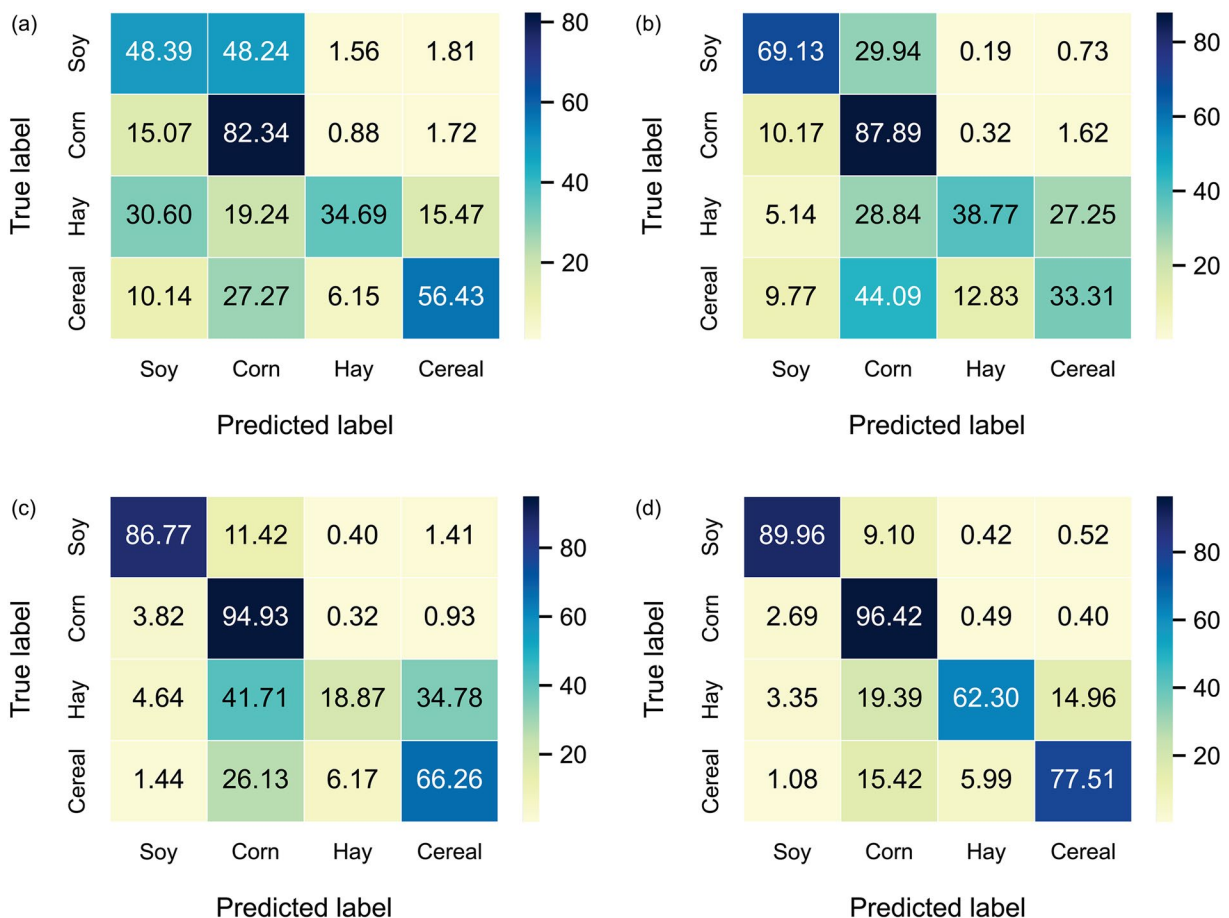

Figure 6. The confusion matrices for the final classification maps of single-date and multi-date CP data. (a) July 1, (b) July 30, (c) August 27, and (d) July 1 + July 30 + August 27.

Table 7. User's and producer's accuracies for single-date and multi-date CP data in percent.

	Soy		Corn		Hay		Cereal	
Dates	UA	PA	UA	PA	UA	PA	UA	PA
July 1	59.64	48.39	70.75	82.34	50.67	34.69	68.64	56.43
July 30	76.94	69.13	76.67	87.89	56.41	38.77	54.99	33.31
August 27	91.98	86.77	87.02	94.93	50.25	18.87	69.33	66.26
July 1 + July 30 + August 27	94.38	89.96	91.20	96.42	75.18	62.30	86.31	77.51

Table 8. Classification results for each CP feature obtained from multi-date CP data.

				Soy		Corn		Hay		Cereal	
Features	OA	Kappa	F1-score	UA	PA	UA	PA	UA	PA	UA	PA
Intensities	84.88	0.73	84.52	88.30	81.85	85.40	92.86	66.07	48.68	75.17	64.05
Stokes parameters	90.94	0.84	90.76	94.88	89.27	90.75	96.62	75.60	60.20	84.16	76.87
Stokes child parameters	70.62	0.46	68.61	68.57	58.87	71.27	86.08	55.67	4.71	73.80	49.98
m-chi	89.63	0.82	89.45	92.59	87.32	89.68	95.42	73.62	60.76	85.25	76.29
m-delta	88.91	0.81	88.71	92.17	86.42	89.06	95.11	71.57	58.98	83.27	74.13
H/A/Alpha	77.62	0.59	74.98	79.11	77.62	77.06	90.45	92.00	0.07	75.02	35.96
RVOG-based	89.63	0.82	89.45	92.59	87.31	89.67	95.42	73.63	60.83	85.30	76.28
Dey et al.	89.53	0.82	89.32	92.63	87.25	89.32	95.54	74.67	59.41	85.69	75.25
Conformity coefficient	58.32	0.16	52.23	54.60	25.54	58.81	88.82	100.0	0.01	65.45	16.25
All 90 CP features	91.20	0.85	91.04	94.38	89.96	91.20	96.42	75.18	62.30	86.31	77.51
Selected CP features	91.14	0.85	90.97	94.59	89.79	91.06	96.49	75.31	62.21	85.68	77.08

together, the OA peaks at 91.20%, with the Kappa Coefficient and F1-Score closely following at 0.84% and 91.04%, respectively, which suggests that leveraging multitemporal CP data enhances the classification performance, yielding better results than any single-date CP data.

Table 7 also demonstrated the UA and PA in percent for single-date and multi-date CP data. Notably, both soy and corn classes demonstrated an upward trend in classification accuracy from July to August, with the highest accuracy observed in the multi-date CP data, i.e., 94.38% and 89.96%, as well as 91.20% and 96.42% for UA and PA of soy and corn classes, respectively. On the other hand, UA and PA of the hay and cereal classes fluctuated over the single-dates but saw a substantial boost when multi-date CP data was employed. Overall, the results underscored the effectiveness of using multi-date CP data in crop classification, as it consistently yields higher accuracy rates than single-date CP data, emphasizing the benefits of leveraging multitemporal CP data for more precise assessments.

To further assess crop classification, we independently classified each set of CP features. Table 8 presents the calculated classification metric values derived from the multi-date CP data. As mentioned, classification accuracy will be notably high when all 90 features are considered. The Stokes parameters stand out with a high OA of 90.94% and a Kappa of 0.84, reflecting their reliability in classification tasks,

further corroborated by a strong F1-score of 90.76%. In contrast, the Stokes child parameters and the Conformity coefficient exhibit lower performance metrics, with OAs of 70.62% and 58.32% and Kappa values of 0.46 and 0.16, respectively. Interestingly, while the m-chi and m-delta features boast high OAs above 88%, the m-chi feature demonstrates a marginally superior performance. The RVOG-based and Dey et al. features also display comparable efficacy, achieving OAs exceeding 89% and Kappa values of 0.82.

Feature importance

Feature importance in the RF classifier provides a clear understanding of which feature brings the most insight into the predictions made by the model. By evaluating the contribution of each feature to the decision trees within the ensemble, RF quantifies the importance based on the improvement each feature provides to the overall prediction accuracy. Essential features significantly improve the model's performance, driving it toward accurate predictions. On the other hand, features with low importance may not significantly impact the model's accuracy or might even be redundant. Since the number of CP features we used for the classification task is relatively high, i.e., 90 features, we only demonstrated the top 30 features in Figure 7. The feature importance analysis derived from the RF classification for crop mapping shows

significant insights into the utility of various features extracted from multi-date CP SAR data. The first element of the Stokes parameter, i.e., S_0 August 27, stands out as the most crucial feature, indicating its significant role in differentiating between crops.

Additionally, features from the m-chi and m-delta decomposition play a vital role in the classification, underscoring their potential to extract meaningful information crucial for crop differentiation. In contrast, the RVOG-based and Dey et al. decompositions features seem less critical, suggesting they might be less influential for this classification task. The intensity features also moderately influence the importance scale, signifying their moderate contribution to the crop mapping process. Additionally, even though the Stokes child parameters were not among the most prominent features, they remain essential. Their recurring appearance over various dates highlights their significance in providing valuable information alongside the primary influential features.

Correlation assessment of CP features

The Spearman correlation coefficient is a nonparametric measure of rank correlation that assesses the strength and direction of the monotonic relationship between two variables without making any assumptions about their distribution. The coefficient's values range from -1 to $+1$, where $+1$ denotes a perfect positive monotonic relationship, 0 no monotonic relationship, and -1 a perfect negative monotonic relationship. The Spearman correlation coefficient is an invaluable statistical tool for measuring the degree of correlation between different remotely sensed variables, e.g., each pair of CP features. Here, we use the absolute value of the Spearman correlation coefficient since we are interested in measuring the strength of the relationship between various CP features, regardless of whether the relationship is positive or negative. This approach allows us to focus on how closely related the variables are without considering the
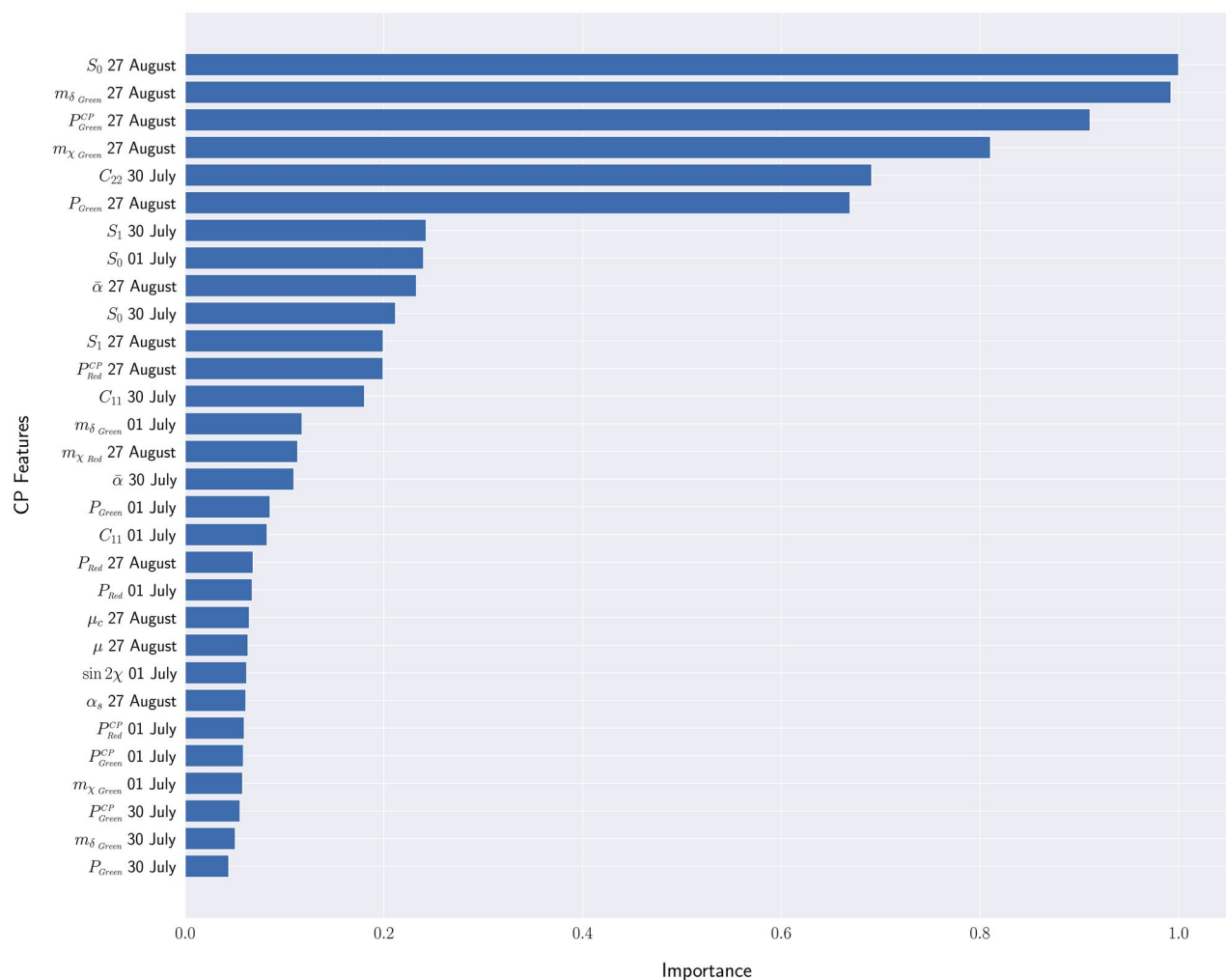

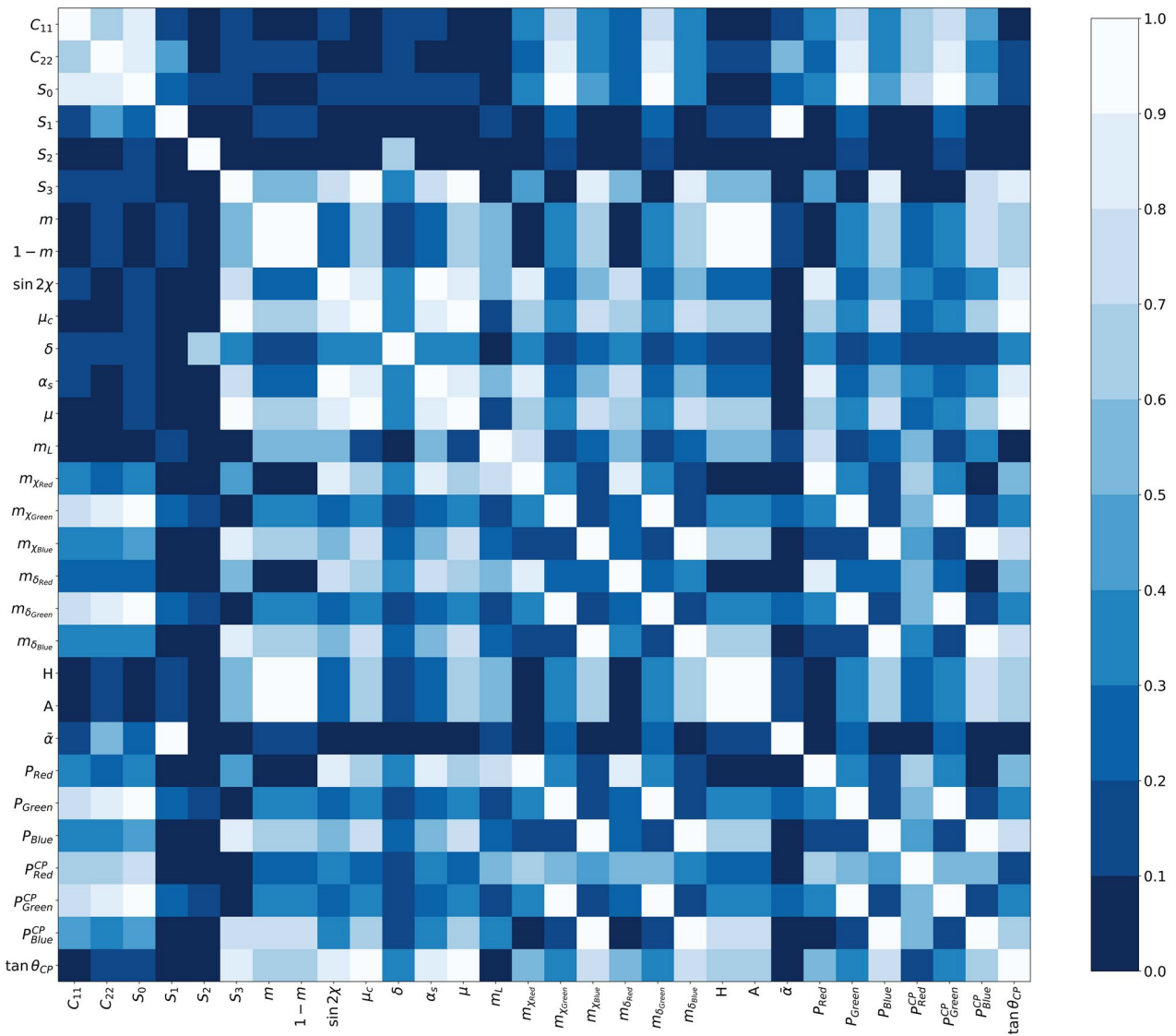**Figure 7.** The top 30 important CP features.

Figure 8. The absolute value of the Spearman correlation computed between various CP features.

direction of their relationship, and it can help identify strong correlations among the features.

We only indicate the Spearman correlation for August 27, 2021 since it was the most crucial date in the crop classification. Figure 8 illustrates the absolute value of the Spearman correlation between various extracted CP features. Upon visual inspection of this figure, it is evident that several CP features exhibit strong correlations with each other. Features related to the volume scattering (i.e., $m_{\chi_{Green}}$, $m_{\delta_{Green}}$, P_{Green}, and P_{Green}^{CP} in the m-chi, m-delta, RVOG-based, and Dey et al. decompositions respectively) is an example of this correlation. We can also see that these features are correlated in many cases. Hence, it is plausible that they could be capturing similar information about the scattering mechanisms present within the observed scene. As a result, this could imply that one feature could be used as a substitute for the others, reducing the dimensionality of the feature set without significant loss of information. Additionally, we can see a high degree of correlation between the Stokes child parameters in most cases.

Crop classification based on selected CP features

In this subsection, we select CP features exhibiting low correlation to classify multi-date CP data. Specifically, we opt for intensities, all Stokes parameters, and three Stokes child parameters: m, $\sin 2\chi$, and δ. Furthermore, We solely utilize the m-chi decomposition. In total, 27 CP features were employed for the multi-date crop classification. Table 8 summarizes the classification results using these selected CP features. Remarkably, the OA, Kappa coefficient, F1-score, UA, and PA were nearly identical to the results obtained when all 90 CP features were utilized.

This observation proves a high correlation among many CP features, providing redundant information as discussed in subsections Feature importance and Correlation assessment of CP features. Consequently, we can still achieve better classification results by discarding these correlated features and focusing solely on the selected CP features.

Conclusion

This research aimed to underscore the potential of multitemporal CP data provided by the RCM for crop classification. The study area was located in southern Quebec, Canada, and three ascending RCM CP datasets acquired on July 1, July 30, and August 27, 2021 were used in this study. These datasets have a 5-m resolution and were obtained in StripMap mode. The dataset also comprises four distinct classes: soy, corn, hay, and cereal. The CP data was processed to derive the 2×2 C2 covariance matrix. A diverse set of CP features, including Stokes parameters, Stokes child parameters, $m-\chi, m-\delta, H/A/Alpha$, RVOG-based, and Dey et al. decompositions, were stacked together with intensity values, resulting in a stack containing 90 features.

Utilizing the RF classifier, a notable machine learning model recognized for its efficacy in classification tasks, the multitemporal CP data yielded an OA, Kappa Coefficient, and F1-score of ~91, 0.84, and 91%, respectively. The experimental results indicated that the multi-date CP data classification performance significantly surpassed that of single-date analysis (i.e., classification of July 1, July 30, and August 27 dates individually), affirming that multi-date observations provide a more comprehensive reflection of crop status over time. The superiority of multi-date over single-date classification was further corroborated by the progressive improvement in User's and Producer's accuracies across the timeline of data acquisition, with the multi-date analysis providing the most reliable results. Moreover, analyzing the importance of each feature showed that the feature derived from the data collected on August 27 played a pivotal role in the efficacy of the RF classifier.

The Spearman correlation coefficient was utilized to assess CP feature correlations. The analysis revealed significant correlations between the m-chi, m-delta, RVOG-based, and Dey et al. decompositions. A notable correlation was also observed among the Stokes child parameters. When employing intensities, Stokes parameters, selected Stokes child parameters, and the m-chi decomposition for classification, the results indicated that nearly the same level of classification accuracy could be achieved when all available CP features were utilized.

It is important to acknowledge certain limitations. Our analysis was constrained by the availability of CP data, so we used only three dates spaced approximately a month apart. While these data points were selected to capture key phenological stages, they do not fully exploit the RCM's impressive 4-day revisit capability, potentially limiting our temporal analysis's depth. To address this limitation, we plan to incorporate a more comprehensive dataset in our future work that spans more frequent temporal intervals, leveraging the full capabilities of the RCM. Furthermore, the challenge of spatial autocorrelation, which optimistically increases classification accuracy, highlights the need for advanced methodological approaches to ensure the robustness of classification results. Thus, we aim to explore sophisticated Deep Learning models in our future work to mitigate issues related to spatial autocorrelation and enhance the reliability of our classification outcomes. These steps will be crucial in advancing our understanding of crop dynamics and improving the accuracy and applicability of CP data for agricultural monitoring.

Disclosure statement

No conflict of interest was reported by the author(s).

References

Billah, M., Islam, A.K.M.S., Mamoon, W.B., and Rahman, M.R. 2023. "Random forest classifications for landuse mapping to assess rapid flood damage using Sentinel-1 and Sentinel-2 data." *Remote Sensing Applications: Society and Environment*, Vol. 30: pp. 100947. doi:10.1016/j.rsase.2023.100947.

Breiman, L. 2001. "Random forests." *Machine Learning*, Vol. 45 (No. 1): pp. 5–32. doi:10.1023/A:1010933404324.

Brisco, B., Li, K., Tedford, B., Charbonneau, F., Yun, S., and Murnaghan, K. 2013. "Compact polarimetry assessment for rice and wetland mapping." *International Journal of Remote Sensing*, Vol. 34 (No. 6): pp. 1949–1964. doi: 10.1080/01431161.2012.730156.

Brisco, B., Mahdianpari, M., and Mohammadimanesh, F. 2020. "Hybrid compact polarimetric SAR for environmental monitoring with the RADARSAT constellation mission." *Remote Sensing*, Vol. 12 (No. 20): pp. 3283. doi:10.3390/rs12203283.

Canadian Space Agency. 2023. *RADARSAT Technical Features – Characteristics*. https://www.asc-csa.gc.ca/eng/satellites/radarsat/technical-features/characteristics.asp. Accessed April 14, 2023.

Charbonneau, F.J., Brisco, B., Raney, R.K., McNairn, H., Liu, C., Vachon, P.W., Shang, J., et al. 2010. "Compact polarimetry overview and applications assessment." *Canadian Journal of Remote Sensing*, Vol. 36 (No. sup2): pp. S298–S315. doi:10.5589/m10-062.

Chirakkal, S., Haldar, D., and Misra, A. 2017. "Evaluation of hybrid polarimetric decomposition techniques for winter crop discrimination." *Progress in Electromagnetics Research M*, Vol. 55: pp. 73–84. doi:10.2528/PIERM17011603.

Cloude, S. 2009. *Polarisation: Applications in Remote Sensing*. New York: OUP Oxford.

Cloude, S.R., and Pottier, E. 1996. "A review of target decomposition theorems in radar polarimetry." *IEEE Transactions on Geoscience and Remote Sensing*, Vol. 34 (No. 2): pp. 498–518. doi:10.1109/36.485127.

Cloude, S.R., Goodenough, D.G., and Chen, H. 2012. "Compact decomposition theory." *IEEE Geoscience and Remote Sensing Letters*, Vol. 9 (No. 1): pp. 28–32. doi:10.1109/LGRS.2011.2158983.

Collett, E. 2005. *Field Guide to Polarization*. Bellingham, WA: SPIE.

Dasari, K., and Lokam, A. 2018. "Exploring the capability of compact polarimetry (hybrid pol) c band RISAT-1 data for land cover classification." *IEEE Access*, Vol. 6: pp. 57981–57993. doi:10.1109/ACCESS.2018.2873348.

Dey, S., Bhattacharya, A., Ratha, D., Mandal, D., and Frery, A.C. 2021. "Target Characterization and Scattering Power Decomposition for Full and Compact Polarimetric SAR Data." *IEEE Transactions on Geoscience and Remote Sensing*, Vol. 59 (No. 5): pp. 3981–3998. doi:10.1109/TGRS.2020.3010840.

Dingle Robertson, L., McNairn, H., Jiao, X., McNairn, C., and Ihuoma, S.O. 2022. "Monitoring crops using compact polarimetry and the RADARSAT constellation mission." *Canadian Journal of Remote Sensing*, Vol. 48 (No. 6): pp. 793–813. doi:10.1080/07038992.2022.2121271.

Dubois-Fernandez, P.C., Souyris, J.-C., Angelliaume, SÉbastien., and Garestier, F. 2008. "The compact polarimetry alternative for spaceborne SAR at low frequency." *IEEE Transactions on Geoscience and Remote Sensing*, Vol. 46 (No. 10): pp. 3208–3222. doi:10.1109/TGRS.2008.919143.

European Space Agency. 2024. *Sentinel Application Platform (SNAP)*. https://earth.esa.int/eogateway/tools/snap.

Government and Municipalities of Québec. 2023. *Database of Declared Agricultural Plots and Productions (BDPPAD)*. https://open.canada.ca/data/en/dataset/1995c916-81e5-4eed-9142-c3763423dfc8. Accessed July 13, 2023.

Ioannidou, M., Koukos, A., Sitokonstantinou, V., Papoutsis, I., and Kontoes, C. 2022. "Assessing the added value of Sentinel-1 PolSAR data for crop classification." *Remote Sensing*, Vol. 14 (No. 22): pp. 5739. doi:10.3390/rs14225739.

Jafarzadeh, H., Verma, A., Mahdianpari, M., Bhattacharya, A., and Homayouni, S. 2024. "Enhanced crop discrimination and monitoring using compact-polarimetric SAR signature analysis from RADARSAT constellation mission." *IEEE Journal of Selected Topics in Applied Earth Observations and Remote Sensing*, Vol. 17: pp. 6308–6327. doi:10.1109/JSTARS.2024.3366883.

Kobayashi, N., Tani, H., Wang, X., and Sonobe, R. 2020. "Crop classification using spectral indices derived from Sentinel-2A imagery." *Journal of Information and Telecommunication*, Vol. 4 (No. 1): pp. 67–90. doi:10.1080/24751839.2019.1694765.

La Financière agricole du Québec. 2023. *Base de données des parcelles et productions agricoles déclarées (BDPPAD)*. https://www.fadq.qc.ca/documents/donnees/base-de-donnees-des-parcelles-et-productions-agricoles-declarees/. Accessed July 13, 2023.

Lee, J.-S., and Pottier, E. 2017. *Polarimetric Radar Imaging: From Basics to Applications*. Boca Raton: CRC Press.

Mahdianpari, M., Mohammadimanesh, F., McNairn, H., Davidson, A., Rezaee, M., Salehi, B., Homayouni, S., et al. 2019. "Mid-season crop classification using dual-, compact-, and full-polarization in preparation for the RADARSAT Constellation Mission (RCM)." *Remote Sensing*, Vol. 11 (No. 13): pp. 1582. doi:10.3390/rs11131582.

Omia, E., Bae, H., Park, E., Kim, M.S., Baek, I., Kabenge, I., Cho, B.-K., et al. 2023. "Remote sensing in field crop monitoring: A comprehensive review of sensor systems, data analyses and recent advances." *Remote Sensing*, Vol. 15 (No. 2): pp. 354. doi:10.3390/rs15020354.

Orynbaikyzy, A., Gessner, U., and Conrad, C. 2022. "Spatial transferability of random forest models for crop type classification using Sentinel-1 and Sentinel-2." *Remote Sensing*, Vol. 14 (No. 6): pp. 1493. doi:10.3390/rs14061493.

Pedregosa, F., Varoquaux, G., Gramfort, A., Michel, V., Thirion, B., Grisel, O., Blondel, M., Prettenhofer, P., Weiss, R., Dubourg, V., Vanderplas, J., Passos, A., Cournapeau, D., Brucher, M., Perrot, M., and Duchesnay, E. 2011. "Scikit-learn: Machine learning in Python." *Journal of Machine Learning Research*, Vol. 12 (No. 85): pp. 2825–2830.

Raney, R.K. 2006. "Dual-polarized SAR and stokes parameters." *IEEE Geoscience and Remote Sensing Letters*, Vol. 3 (No. 3): pp. 317–319. doi:10.1109/LGRS.2006.871746.

Raney, R.K. 2007. "Hybrid-polarity SAR architecture." *IEEE Transactions on Geoscience and Remote Sensing*, Vol. 45 (No. 11): pp. 3397–3404.

Raney, R.K. 2019. "Hybrid dual-polarization synthetic aperture radar." *Remote Sensing*, Vol. 11 (No. 13): pp. 1521. doi:10.3390/rs11131521.

Raney, R.K., Brisco, B., Dabboor, M., and Mahdianpari, M. 2021. "RADARSAT Constellation Mission's operational polarimetric modes: A user-driven radar architecture." *Canadian Journal of Remote Sensing*, Vol. 47 (No. 1): pp. 1–16. doi:10.1080/07038992.2021.1907566.

Raney, R.K., Cahill, J.T.S., Patterson, G.W., and Bussey, D.B.J. 2012. "The m-chi decomposition of hybrid dual-polarimetric radar data." 2012 IEEE International Geoscience and Remote Sensing Symposium, Munich, Germany, pp. 5093–5096.

Robertson, L.D., Davidson, A., McNairn, H., Hosseini, M., and Mitchell. S. 2019. "Compact polarimetry for agricultural mapping and inventory: Preparation for RADARSAT constellation mission." IGARSS 2019–2019 IEEE International Geoscience and Remote Sensing Symposium, Yokohama, Japan, pp. 5851–5854. IEEE.

Shang, J., Liu, J., Chen, Z., McNairn, H., and Davidson, A. 2022. "Recent advancement of synthetic aperture radar (SAR) systems and their applications to crop growth monitoring."

In *Recent Remote Sensing Sensor Applications*, edited by M. Marghany. Rijeka: IntechOpen, Chap. 2.

Sheykhmousa, M., Mahdianpari, M., Ghanbari, H., Mohammadimanesh, F., Ghamisi, P., and Homayouni, S. 2020. "Support vector machine versus random forest for remote sensing image classification: A meta-analysis and systematic review." *IEEE Journal of Selected Topics in Applied Earth Observations and Remote Sensing*, Vol. 13: pp. 6308–6325. doi:10.1109/JSTARS.2020.3026724.

Sishodia, R.P., Ray, R.L., and Singh, S.K. 2020. "Applications of remote sensing in precision agriculture: A review." *Remote Sensing*, Vol. 12 (No. 19): pp. 3136. doi:10.3390/rs12193136.

Thompson, A.A. 2010. "Innovative capabilities of the RADARSAT constellation mission." 8th European Conference on Synthetic Aperture Radar.

Truong-Loi, M.-L., Freeman, A., Dubois-Fernandez, P. C., and Pottier, E. 2009. "Estimation of soil moisture and Faraday rotation from bare surfaces using compact polarimetry." *IEEE Transactions on Geoscience and Remote Sensing*, Vol. 47 (No. 11): pp. 3608–3615.

Uppala, D., Venkata, R.K., Poloju, S., Venkata Rama, S.M., and Dadhwal, V.K. 2016. "Discrimination of maize crop with hybrid polarimetric RISAT1 data." *International Journal of Remote Sensing*, Vol. 37 (No. 11): pp. 2641–2652. doi:10.1080/01431161.2016.1184353.

Van Beijma, S., Comber, A., and Lamb, A. 2014. "Random forest classification of salt marsh vegetation habitats us-ing quad-polarimetric airborne SAR, elevation and optical RS data." *Remote Sensing of Environment*, Vol. 149: pp. 118–129. doi:10.1016/j.rse.2014.04.010.

Wu, B., Zhang, M., Zeng, H., Tian, F., Potgieter, A.B., Qin, X., Yan, N., et al. 2022. "Challenges and opportunities in remote sensing-based crop monitoring: A review." *National Science Review*, Vol. 10 (No. 4): pp. nwac290. doi:10.1093/nsr/nwac290.

Xie, L., Zhang, H., Li, H., and Wang, C. 2015. "A unified framework for crop classification in southern China using fully polarimetric, dual polarimetric, and compact polarimetric SAR data." *International Journal of Remote Sensing*, Vol. 36 (No. 14): pp. 3798–3818. doi:10.1080/01431161.2015.1070319.

Yang, S., Gu, L., Li, X., Jiang, T., and Ren, R. 2020. "Crop classification method based on optimal feature selection and hybrid CNN-RF networks for multi-temporal remote sensing imagery." *Remote Sensing*, Vol. 12 (No. 19): pp. 3119. doi:10.3390/rs12193119.

You, B., Yang, J., Yin, J., and Xu, B. 2014. "Decomposition of the Kennaugh matrix based on a new norm." *IEEE Geoscience and Remote Sensing Letters*, Vol. 11 (No. 5): pp. 1000–1004. doi:10.1109/LGRS.2013.2284336.

Zhang, H., Xie, L., Wang, C., Wu, F., and Zhang, B. 2014. "Investigation of the capability of decomposition of compact polarimetric SAR." *IEEE Geoscience and Remote Sensing Letters*, Vol. 11 (No. 4): pp. 868–872.